

1. Introduction

The variability of the X-ray emission is one of the basic characteristics of Active Galactic Nuclei (AGN). Well established since the EXOSAT observations (Pounds 1985), the variability is expected to be an important tool in the study of the accretion process, although its aperiodic noise-like character was early on recognized as a source of interpretation difficulty (McHardy & Czerny 1987; Lawrence et al. 1987).

The phenomenological approach to X-ray variations has brought significant information on the properties of the lightcurves, such as their power spectral density (e.g. Markowitz et al. 2003; McHardy et al. 2005) and their process nonlinearity (Uttley et al. 2005). Nevertheless, the physical processes behind the observed variability have not yet been fully understood. The same is true for accreting galactic black holes. The main source of the ambiguity is that several different models can account for the average radiation spectra, e.g. the 'hot inner flow model' (Ichimaru 1977; Narayan & Yi 1994; Kato et al. 2004; Sobolewska et al. 2004a), the 'continuous corona model' (Liang & Price 1977; Bisnovatyi-Kogan & Blinnikov 1977; Czerny & Elvis 1987; Haardt & Maraschi 1991; Czerny et al. 2003; Merloni 2003), the 'patchy corona model' (Galeev et al. 1979; Haardt et al. 1994; Stern et al. 1995; Ross et al. 1999; Nayakshin et al. 2000; Sobolewska et al. 2004b), or the 'jet-basis model' (Henri & Pelletier 1991; Markoff et al. 2005). Several models can also account for the power density spectra, e.g. the 'shot model' (Lehto 1989), the 'self-organized critical state model' (Mineshige et al. 1994), or the 'traveling perturbations model' (Lyubarskii 1997; King et al. 2004). Apparently, it is impossible to uniquely determine the accretion flow geometry on the basis of power spectra or from the analysis of the mean spectral shape alone.

Therefore, a 2-D approach is needed, which would combine the time and the energy dependence. Such an approach was pioneered in the context of binary black holes using various techniques, e.g., phase lags (Miyamoto et al. 1988; Cui et al. 1997), correlation functions (Nolan et al. 1981; Poutanen & Fabian 1999), coherence functions (Vaughan & Nowak 1997), frequency resolved spectra (Gilfanov et al. 2000; Zycki 2002; Zycki 2003), wavelet analysis (Lachowicz & Czerny 2005). Now the appropriate data is starting to be available for AGN (e.g. Yaqoob et al. 2003; Kaastra et al. 2004; Ponti et al. 2004; Markowitz 2005). We therefore concentrate on modeling the energy-dependent fractional variability amplitude (Vaughan et al. 2003). Long light curves obtained from Chandra and XMM-Newton satellites allow us to determine this function for a few AGN. Such detailed information provides a challenge to the models.

In the present paper, we consider the magnetic flare model of the X-ray emission, suggested by Galeev et al. (1979) in the context of Cyg X-1, and further developed in various directions by several authors, both in the context of galactic sources (Poutanen & Fabian 1999; Beloborodov

1999) and AGN (Haardt et al. 1994; di Matteo 1998; Merloni & Fabian 2001; Torricelli-Ciamponi et al. 2005). In this picture, the magneto-rotational instability (MRI) operating in the disk occasionally leads to the rise of large magnetic loops high above the disk surface. Field reconnection occurs in this region and leads to the creation of localized regions of hot plasma (flares). The flares are cooled by Comptonizing the disk emission, which produces a power law X-ray radiation, customarily called primary emission. A fluctuating number of flares depending on various parameters is supposed to be responsible for the observed AGN variability. Recent 3-D simulations of the magneto-rotational instability within the disk seem to support such a picture (e.g. Miller & Stone 2000; Turner 2004), but simulations including the Compton cooling are still to be done.

The hard X-ray emission of a flare leads to the creation of a hot spot at the disk surface where the X-ray emission is reflected/reprocessed. The combined emission of all spots thus constitutes the so-called reflected component in the total X-ray spectrum, and the issue of the reprocessing of the incident X-ray radiation by the disk surface has been extensively studied (e.g. Lightman & White 1988; Ross & Fabian 1993; Zycki et al. 1994; Nayakshin et al. 2000; Ballantyne et al. 2001; Różańska et al. 2002).

Here, we extend our previous work on this subject (Czerny et al. 2004). We improve our description of the spot emission by taking its dependence on the distance from the spot center and on the local emission direction into account. We use these new computations to model the standard fractional variability amplitude as well as the point-to-point fractional variability amplitude. We compare the results to observational data of MCG-6-30-15.

2. The model

2.1. Radiative transfer within the spot

Let the flare be located at a certain height above an accretion disk. It illuminates the disk surface. We assume that the flare source is very compact and approximate it by an isotropic, point-like source. The emitted spectrum is of a power law shape, with the photon index $\Gamma = 1.9$, extending from 1 eV to 100 keV.

The reprocessed emission depends on the distance from the flare. Therefore, we divide the patch into concentric rings (see Fig. 1). Within each ring, the incident angle of the hard X-ray illumination and irradiating flux is approximately constant. It is convenient not to parameterize the rings by their radial distance from the projected position of the flare (spot-center), but instead by μ , which is the cosine of the incident angle θ of the irradiating flux (see Fig. 1). We vary $\mu = \cos \theta$ in constant steps of 0.1, ensuring that all rings intercept the same fraction of the total illuminating flux.

The reflected spectrum of each ring is calculated for five values of the local emission angle, ψ , measured with respect to the disk axis. We choose equal steps in $\cos \psi$

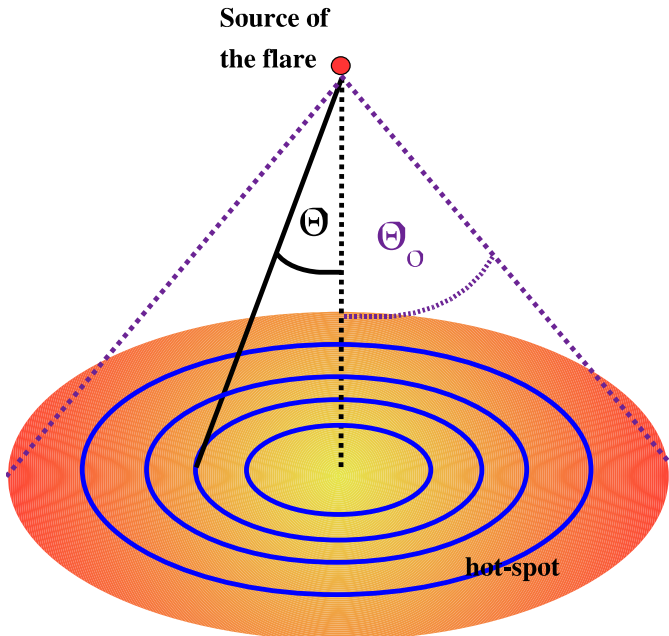


Fig. 1. Spot approximated by five rings below a flare. In each of the rings, the reflected spectrum is calculated for the corresponding incident angle θ of the X-ray radiation and the ionization parameter at the surface.

from 0.1 to 0.9. The local radiation spectrum is computed accurately by performing radiative transfer simulations in plane-parallel approximation. The vertical structure of the illuminated disk is computed using the code of Różańska et al. (2002). Following an argument made by Collin et al. (2003), we assume that the total flare duration is significantly shorter than the characteristic timescale for the restoration of the hydrostatic equilibrium in the suddenly irradiated disk. We thus use the vertical density profile of the disk as computed before the flare turns on.

The local radiative transfer computations are conducted by coupling the codes TITAN and NOAR, as described in Dumont et al. (2000) and updated in Dumont et al. (2003). To model the accretion disk atmosphere, we assume a vertically stratified, plane-parallel medium being irradiated by hard X-ray radiation from above its upper surface. From underneath, low-temperature black-body radiation is added to account for the heating of the underlying disk. The computations are performed for a $10^8 M_\odot$ black hole with a disk accretion rate of 0.001 of the Eddington accretion rate. A distance of $18 R_g$ ($R_g = GM/c^2$) from the black hole is assumed, and the ratio of the incident flux to the disk flux equals 144 at the center of the spot. Details of these calculations are described in Goosmann et al. (2006).

The overall response of the irradiated material to the incident flux is in agreement with known results: a hot layer forms at the top of the disk atmosphere, that is roughly at the inverse Compton temperature, followed by a steep transition to colder, less ionized layers. Such behavior is due to the requirement of the hydrostatic equi-

librium (Field 1965; Krolik et al. 1981; Raymond 1993; Ko & Kallman 1994; Różańska & Czerny 1996; Nayakshin et al. 2000; Ballantyne et al. 2001; Różańska et al. 2002). However, the horizontal stratification of the spot introduced in our model brings new aspects to the resulting reprocessing: we include the fact that the disk surface is most strongly irradiated directly below the flare, while the irradiating flux decreases and the incident angle of the irradiation increases with the distance from the hot spot center. Therefore, the surface inside a hot spot shows a significant radial gradient of its properties, including the locally emitted spectrum. The incident angle and the local incident flux are different in each ring. Large differences between the ring spectra are seen in the soft X-ray band. Spectra from the outer rings are much harder than those from the inner rings, since the reflector there is less ionized. The high-energy parts of the local spectra from all rings are rather similar to each other.

2.2. Ring integration and dependence on the local emission angle

The final spectrum of a spot, for a given local emission direction, is determined by the integration over the rings. Due to the adopted parameterization of the rings, the integration actually reduces to a simple summation. If the flare emission is somehow collimated toward the disk, the outer parts of the hot spot are not irradiated. Therefore, we can treat the opening angle of the irradiating cone as an additional parameter of the model. Here, we adopt a half-opening angle $\Theta_0 = 60^\circ$. This value of Θ_0 corresponds to half of the illuminating flux being reprocessed by the disk medium and also ensures that our calculations remain accurate with respect to the local conditions of the assumed hydrostatic equilibrium. The resulting local spectra are shown in Fig. 2. These ψ -dependent spot spectra are further adopted as representative of computations of a whole accretion disk covered by many spots.

We note that by integrating over the spot surface, we average the spectrum and lose some spatial resolution. We do that in the present model for simplicity. In reality, the properties of the incident and reprocessed radiation change across the spot, which affects the single spot lightcurve. An investigation of this effect is part of a detailed study about individual flare spots (Goosmann et al. 2006). From this study, it follows that in our case the integration over the spot surface does not induce a major error. The intensity of the local spectra at a given emission angle ψ changes regularly across the spot surface and only within a factor of $\sim 2 - 3$. Also, the spectral slope only changes by a factor < 2 .

The shape of the radiation spectrum of a whole spot does not depend strongly on the emission angle ψ , while the overall normalization does. The normalization rises toward higher values of ψ , which represents a limb-brightening effect. The spectrum for all emission angles are much harder than the local spot spectrum used by Czerny

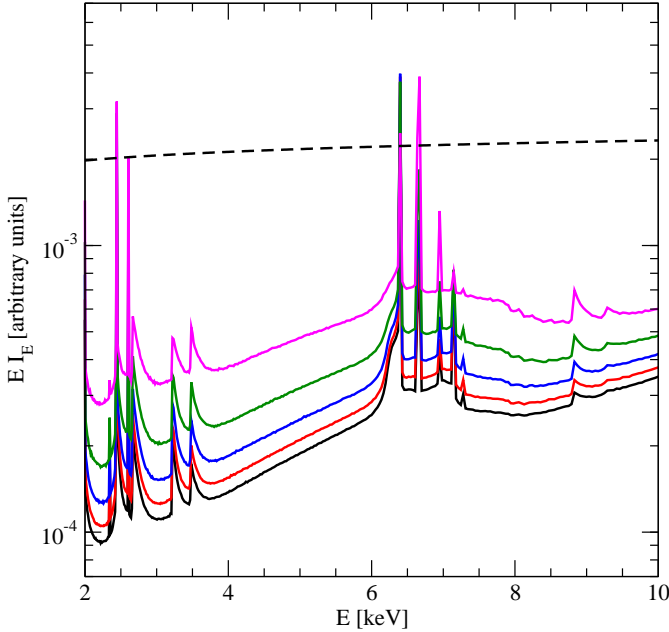


Fig. 2. The spot spectra (intensity) integrated over the rings for 5 values of the emission angle ψ : $\cos \psi = 0.1, 0.3, 0.5, 0.7$, and 0.9 . The upper spectrum is the side view. Parameters adopted: $M = 10^8 M_\odot$, $R = 18 R_g$, $\dot{m}_{disk} = 0.001$, and $L_X/L_d = 144$.

et al. (2004). This is caused by our present assumption of short lasting flares, while Czerny et al. (2004) assumed that the flare duration is long enough for the underlying irradiated disk layers to settle into a new hydrostatic equilibrium.

2.3. Flare distribution across the disk

To define the flare distribution across the disk, we generally follow the simple approach outlined in Czerny et al. (2004). We assume that the spectral shape of all flares is the same, since it consumes too much computer time to repeat such complex computations separately for spots located at various disk radii. On the other hand, we take the fact that the reflected (spot) spectrum shows strong anisotropy of the emissivity (limb-brightening effect) into account.

The source is characterized by n_{mean} , the mean number of all coexisting flares at a given time. The spots are assumed to appear randomly across the disk surface, between the inner radius R_{in} (equal to the marginally stable orbit around a black hole) and the adopted outer radius, R_{out} . The probability distribution of their radial and azimuthal position, (R_i, ϕ_i) , is determined by the general law

$$p(R_i, \phi_i) \equiv p(R_i) p(\phi_i) = \frac{(\gamma_{\text{rad}} + 2) R_i^{\gamma_{\text{rad}} + 1}}{R_{\text{out}}^{\gamma_{\text{rad}} + 2} - R_{\text{in}}^{\gamma_{\text{rad}} + 2}} \times \frac{1}{2\pi}. \quad (1)$$

This distribution reduces to the uniform distribution over the disk surface, if $\gamma_{\text{rad}} = 0$, while positive (negative)

values of γ_{rad} lead to an enhanced number of flares in the outer (inner) disk parts.

The spot radius, R_X , is assumed to be the same for all spots. The flare luminosity and, consequently, the local spot radiation flux generally scales with the flare position, R_i , as

$$F_{\text{inc}} = F_0 \left(\frac{R_i}{R_{\text{in}}} \right)^{-\beta_{\text{rad}}}. \quad (2)$$

The dissipation within the Keplerian disk scales with R^{-3} , so the typical value of β_{rad} is expected to be of that order.

The duration of the flare may also depend on the flare location, so we describe it as

$$t_{\text{life}} = t_{\text{life}_0} \left(\frac{R_i}{R_{\text{in}}} \right)^{\delta_{\text{rad}}}. \quad (3)$$

Here, $\delta_{\text{rad}} = 0$ means that the flare lifetime is independent of the flare location, while for $\delta_{\text{rad}} = 1.5$, the flare lifetime scales with the local Keplerian timescale.

The observational appearance of the source also depends on the duration of the observation (i.e., integration time) and on the inclination angle of an observer with respect to the disk symmetry axis. The value of the black hole mass, M , is another relevant parameter since all distances and timescales scale with M .

The flare distribution is fully described by the model parameters: M , n_{mean} , R_{in} , R_{out} , R_X , F_0 , β_{rad} , γ_{rad} , δ_{rad} , and t_{life_0} . The spot radius R_X can be replaced, if convenient, by the mean X-ray luminosity of the source, L_X .

2.4. Modeling sequences of spectra

The observed properties of the spot distribution are strongly affected by special and general relativistic effects. These effects must be taken into account with the maximum possible accuracy since they account for a significant fraction of the resulting variability. Even a stationary spot on a Keplerian orbit gives a complex variability curve if the relativistic effects are included. Light bending causes a magnification of the emission from a relatively small disk area (located roughly behind the black hole). Flares passing through this area strongly contribute to the rapid fluctuations of the signal.

We apply the code KY (see Dovciak et al. 2004 and Dovciak 2004 for a description) here to compute the relativistic corrections between the local spot spectra and the actually 'observed' ones. The code incorporates all aspects of the light propagation from between the disk surface and a distant observer. It includes the effects of light bending, as well as gravitational and Doppler shifting of the photon energy. The ruling parameters for the relativistic effects are the viewing angle i of a distant observer, measured with respect to the disk normal, and the dimensionless Kerr parameter a of the black hole. The

anisotropic character of the local (ψ -dependent) spot spectra (see Sect. 2.2) is also relevant and included in our modeling.

The resulting disk spectrum seen at a given viewing angle i is based on a combination of various angle-dependent local spot spectra. However, the integration over the disk surface for a large number of hot spots is computationally time-consuming, so that we cannot produce detailed lightcurves for all spots. However, to model the data, such lightcurves are actually not needed because the spectra can only be measured in bins T_{obs} of the typical order of a few thousands of seconds. Therefore, within each time bin, we consider the appearance/disappearance of the hot spots and their motion. Then we construct the emissivity ‘belts’, which represent the traces of the spots on the disk surface over their duration. This method is identical to the one applied in Czerny et al. (2004). Finally, the spectrum $S_k(E)$ of the radiation received by a distant observer within a time bin k , is computed. We calculate N of such sequences for a given flare distribution. Usually we adopt $N = 50$ since this corresponds well to the best observed lightcurves covering a few hundreds of thousands of seconds.

Another modification, introduced in the current model in comparison to the method of Czerny et al. (2004), is the survival of flares between consecutive time bins. Czerny et al. (2004) treated each time bin as being separate from the previous one, and all spot positions were newly generated. This is correct if the time bins do not come from a single, uninterrupted observation or if the effective life time of the flares is shorter than the length of a time bin. In the current modeling, we follow the positions of the hot spots over consecutive time bins. A randomly sampled position, according to an adopted spot distribution, is assigned only to new born flares. This Monte-Carlo sampling also considers an adopted birth rate, which is determined by the mean number of flares, their life time, and by the spatial spot distribution. This parameterization allows an appropriate description of the overall X-ray properties of the source.

2.5. Fractional variability

The obtained radiation spectra sequences allow us to calculate the fractional variability for a given flare distribution. We follow the definition used by Ponti et al. (2004):

$$\hat{F}_{\text{var}}^2(E) = \sum_{k=1}^N \frac{(S_k(E) - \langle S(E) \rangle)^2}{(N-1)\langle S(E) \rangle^2}, \quad (4)$$

where N is the number of time bins, $S_k(E)$ is the integrated radiation spectrum for a single time bin k , and $\langle S(E) \rangle$ is the mean spectrum. We also determine the statistical errors for this determination of \hat{F}_{var} , as it is done for the observed data (see Ponti et al. 2004). Of course the modeled lightcurve is not limited by the S/N ratio, although it is limited by the adopted total duration of the

observation and by the width of the energy channels for the final F_{var} .

By statistical errors, we mean the error determination from a *single* simulated lightcurve. In the simulations, we use a fine energy grid of 800 points in a 2–10 keV energy range. The dimensionless $\hat{F}_{\text{var}}(E)$ is determined at each energy point. When we compare the model to the data, we bin the results using broader energy bins. If n original energy points contribute to the new energy bin centered around E_k , we introduce

$$F_{\text{var}}(E_k) = \frac{\sum_{i=1}^n \hat{F}_{\text{var}}(E_i)}{n}, \quad (5)$$

and the error of this quantity is determined as

$$\delta F_{\text{var}}(E_k) = \left[\frac{\sum_{i=1}^n \hat{F}_{\text{var}}^2(E_i) - n F_{\text{var}}^2(E_k)}{n^2} + \frac{(F_{\text{var}}^2(E_k) + 1) F_{\text{var}}^2(E_k)}{n(N-1)} \right]^{1/2}. \quad (6)$$

The first term in this expression determines the error of the mean value by averaging over the energy bins and assuming an error of $\hat{F}_{\text{var}}(E_i) - F_{\text{var}}(E_k)$ for a given $\hat{F}_{\text{var}}(E_i)$. The second term is the expected statistical error for a normalized variance effectively calculated from $n(N-1)$ points. Both components are necessary, since in the model the values in nearby energy bins are not statistically independent.

2.6. Point-to-point fractional variability

We also calculate the point-to-point fractional variability (Edelson et al. 2002; Vaughan & Fabian 2004), which emphasizes the character of the shortest timescale variation. This quantity is calculated by

$$\hat{F}_{\text{pp}}^2(E) = \sum_{k=1}^{N-1} \frac{4 [S_{k+1}(E) - S_k(E)]^2}{(N-1) [S_{k+1}(E) + S_k(E)]^2}, \quad (7)$$

together with the rebinned version

$$F_{\text{pp}}(E_k) = \frac{\sum_{i=1}^n \hat{F}_{\text{pp}}(E_i)}{n}, \quad (8)$$

and the appropriate statistical errors δF_{pp} . They are computed from the same formula as δF_{var} , replacing $\hat{F}_{\text{var}}(E)$ by $\hat{F}_{\text{pp}}(E)$ in Eqn. 6 and $F_{\text{var}}(E)$ by $F_{\text{pp}}(E)$ respectively. Our definition of F_{pp} is even more local than the one previously used because it adopts the local mean instead of a global mean at each step.

3. Results

In our model setup, the vertical disk structure and the local spectra, as a function of the emission angle ψ , are accurately computed for a distance of $18 R_g$ from the black

hole. These local spectra are then applied to hot spots across the whole disk. On the one hand, this is an important simplification in our modeling. On the other hand, however, it helps to reduce the complexity of the problem. The model setup described in the previous section focuses on investigating the effects on the variability caused by General Relativity, by the radial spot distribution across the disk, and by the anisotropic local spectrum emitted by the spots. The shape of the local spectra for each spot are thus assumed to be independent of the spot location, while their normalization is ruled by the radial emission profile of the disk. Further radial dependencies, like the power of the primary emission illuminating the disk or the hydrostatic equilibrium of the disk atmosphere, are to be considered in future work.

The following presentation of our results starts with a comparison to the previous approach of Czerny et al. (2004) in Sect. 3.1. Then, in Sect. 3.2, we point out the main effects on the variability as a function of the model parameters, and we explain them qualitatively. Finally, in Sect. 3.3, we apply the model to some variability data of the Seyfert-1 galaxy MCG-6-30-15.

3.1. The effect of the spot structure and of the anisotropic spot emission

Since we made two important modifications of the model in comparison to the approach of Czerny et al. (2004), we show the significance of these changes in Fig. 3, for two sets of parameters – one corresponding to a Schwarzschild black hole and one corresponding to a maximally rotating Kerr black hole. The mean number n_{mean} of flares is adjusted so that for both choices of the black hole spin, the variability level is roughly the same (see Sect. 3.2). We compare the results obtained from (a) the code of Czerny et al. (2004), (b) the new code taking into account the cloud survival between the time bins, but with the old spot radiation spectrum, and (c) the new code, considering the spot structure and the angle-dependent spot emission.

The differences between cases (a) and (b) are mainly in the normalization. The survival of the flares between the consecutive time bins enhances the variability since it decreases the randomness in the cloud position. The discrepancy between the two approaches increases with a rising ratio of the flare life time t_{life} to the bin size T_{obs} . The considered examples were calculated for t_{life} being independent from the disk radius ($\delta_{\text{rad}} = 0$). If the radial dependence is strong (e.g. $\delta_{\text{rad}} = 1.5$), the cloud survival also induces some difference in the shape of F_{var} .

The most profound difference is introduced by the change of the local spectrum. Case (c) shows a much stronger energy dependence because the new local reflection spectrum has more prominent spectral features, including the iron $K\alpha$ line (see Sect. 2.2). This is promising in the perspective of reproducing the data. The model of Czerny et al. (2004) predicted a far too shallow energy

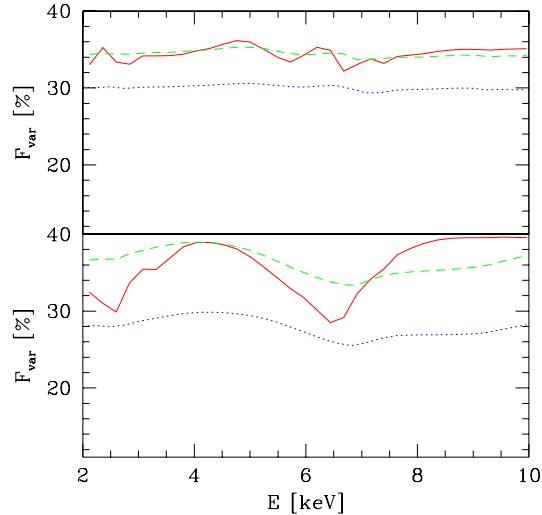


Fig. 3. Fractional variability amplitude for a Schwarzschild black hole (upper panel) and a maximally rotating Kerr black hole (lower panel). Dotted lines: uniform, isotropically radiating spots generated independently in each time bin. Dashed lines: uniform, isotropically radiating spots surviving between consecutive time bins. Continuous lines: present model of non-uniform, non-isotropic spots surviving between consecutive time bins. Other model parameters: $M = 10^8 M_{\odot}$, $L_{\text{X}} = 10^{44} \text{ erg s}^{-1}$, $i = 30^\circ$, $R_{\text{out}} = 50 R_{\text{g}}$, $\beta_{\text{rad}} = 3$, $\gamma_{\text{rad}} = 0$, $\delta_{\text{rad}} = 0$, $t_{\text{life}_0} = 10^5 \text{ s}$, $T_{\text{obs}} = 10^5 \text{ s}$, $N = 300$; and $n_{\text{mean}} = 30$ in the upper panel, while $n_{\text{mean}} = 100$ in the lower panel. The inner radius is equal to the marginally stable orbit adapted to the given choice of the black hole spin. No primary contribution is assumed.

dependence, in comparison with observations of MCG-6-30-15, whereas the new model improves this aspect.

We also made a comparison of the predictions by the new version of the code for the point-to-point variability. In this case, the cloud survival decreases the variability amplitude since, for the adopted model parameters, about half of the clouds survive from one time bin to another and do not contribute much to the point-to-point variability. Some effect is also seen in the shape of $F_{\text{pp}}(E)$ (see Fig. 4).

Furthermore, we calculated $F_{\text{var}}(E)$ and $F_{\text{pp}}(E)$, taking into account the contribution of the primary emission from the flare, with a relative level, as expected for isotropic flare emission. In these cases, the energy dependence of the variability is weak and comparable to the level obtained by Czerny et al. (2004). Although in the new approach the energy dependence in the spot emission variability is stronger, the spot spectrum contributes less to the total (primary plus spot) spectrum due to the less ionized reflecting medium. The two effects roughly compensate for each other and, for an isotropic primary, the

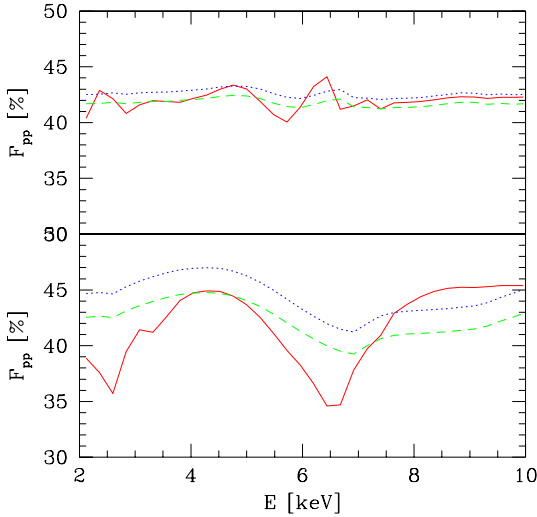


Fig. 4. Point-to-point fractional variability amplitude for a Schwarzschild black hole (upper panel) and a maximally rotating Kerr black hole (lower panel). Dotted lines: uniform, isotropically radiating spots generated independently in each time bin. Dashed lines: uniform, isotropically radiating spots surviving between consecutive time bins. Continuous lines: present model of non-uniform, non-isotropic spots surviving between consecutive time bins. The other parameters of the models are as for Fig. 3.

variations in $F_{\text{var}}(E)$ are again around a mean variability level of about 2%.

3.2. The dependence of the fractional variability on the model parameters

The mean number n_{mean} of flares mostly affects the overall normalization of F_{var} , as does the flare life-time distribution t_{life} : larger values of t_{life} require higher values of n_{mean} to achieve the same overall variability level. The important ruling parameter for the variability in this context is the frequency of flare onsets and endings, which directly determines the fluctuations of the lightcurve. If n_{mean} is high, more onsets and endings per unit time happen and the averaging effect reduces the variability. The lifetime of a single flare acts in the opposite direction. The longer an individual flare lives, the less flares set on or end per unit time.

Suppression of F_{var} at ~ 6.5 keV appears if the radiation is strongly concentrated toward the center. We see such a trend in models with $\delta_{\text{rad}} = 0$, if the spot brightness radially decreases as the standard disk dissipation rate ($\beta_{\text{rad}} = 3$) and the flares are distributed uniformly across the disk surface ($\gamma_{\text{rad}} = 0$). We show an example of this behavior in Fig. 3 (continuous line). If β_{rad} is con-

siderably larger (e.g. $\beta_{\text{rad}} \sim 4.5$), the same pattern is seen even for flare life times scaling with the local Keplerian value ($\delta_{\text{rad}} = 1.5$). This behavior can be qualitatively understood from the following considerations: the $\text{K}\alpha$ line emitted from the innermost spots is relativistically broadened and Doppler-shifted according to the local orbital velocity vector. Since the life-time of a flare close to the marginally stable orbit is, in general, a significant fraction of the orbital period, the line emitted by one spot will shift smoothly in energy around the line centroid. As the line is also strongly relativistically broadened, its shape is rather flat around the centroid, which hence exhibits less variability than do the much steeper wings. In addition to that, there is a contribution to the iron $\text{K}\alpha$ line from outer parts of the disk, and its persistent presence further supports the drop in F_{var} around 6.5 keV. The features in the variability spectrum are thus mainly determined by the relatively few innermost hot spots for which the reprocessed spectrum is more strongly modified by the general relativistic effects.

The parameters γ_{rad} and δ_{rad} act predominantly in the same way, since having more flares at larger distances is roughly equivalent to flares lasting longer at large radii. However, the effect of the two parameters is not strictly identical. The situation is similar with β_{rad} and γ_{rad} : a decrease in β_{rad} has a similar effect as a decrease in γ_{rad} . We should add here that, to a certain extent, the timescale t_{life} also influences the energy dependence of F_{var} . If the timescale is too short, the energy dependence in the variability is smeared, which is again due to the large number of onsets and endings of the hot spots.

In summary, the most important property of a given parameter set is the sum of the parameters, $2 + \gamma_{\text{rad}} + \delta_{\text{rad}} - \beta_{\text{rad}}$, which represents the index of an effective radial distribution of energy generation. If this value is negative, the model is likely to show a suppression of the variability around 6 keV. If the value is positive, the model is likely to show complex behavior around 6 keV in F_{var} , as seen in Fig. 5, and an enhanced variability at ~ 6.5 keV in F_{pp} , as seen in Fig. 7. However, to some extent the specific individual values of all parameters are also important.

As mentioned above, the position of the features in F_{var} and their shape strongly depend on the relativistic effects modifying the spectrum of the inner hot spots. The observed features thus constrain both the inclination angle i of the disk and the Kerr black hole parameter, a . A larger inclination tends to move the features toward higher energies, while a faster black hole rotation produces slightly broader and much deeper features. This is due to the effect that the marginally stable orbit of a rotating black hole is smaller, and thus the hot spots can exist at a closer distance to the event horizon. Therefore, if any features are present in F_{var} , they can be used effectively to constrain a and i .

3.3. Comparison to the special case of MCG-6-30-15

3.3.1. Observational data and fixed model parameters

Two long X-ray exposures were obtained with XMM-Newton for the Seyfert-1 galaxy MCG-6-30-15: one observation lasting 95 ks was performed in June 2000 (Wilms et al. 2001), and the second one lasting about 325 ks was done in July 2001 (Fabian et al. 2002). The time variability in the data from 2000 was analyzed in detail by Ponti et al. (2004), while the time variability in the data from 2001 was studied by Vaughan & Fabian (2004).

We attempt to reproduce the shape of the fractional variability amplitude obtained by Ponti et al. (2004; see their Fig. 2 and Fig. 6 in this paper). We also derive the point-to-point fractional variability amplitude for the same data sequence. In our simulations, we adopt a fixed value $T_{\text{obs}} = 6146$ s, as was done for the computations of F_{var} during the data analysis by Ponti et al. (2004). The number of time bins in the F_{var} calculations is $N = 16$, which is appropriate for the data length. F_{pp} is calculated from the same data using 1000 s bins, so in modeling F_{pp} , we take $T_{\text{obs}} = 1000$ s, and the number of points increases to $N = 100$ to represent the data length correctly. We adopt $10^7 M_{\odot}$ for the mass and 8×10^{43} erg s $^{-1}$ for the X-ray luminosity of the source. We fix the outer disk radius somewhat arbitrarily at $R_{\text{out}} = 50 R_{\text{g}}$. In most cases, we assume $i = 30^\circ$, a Kerr parameter of $a = 0.95$, and $\gamma_{\text{rad}} = 0$.

3.3.2. Intrinsic randomness of the model

The most noticeable property of the model is the considerable randomness in the results for some sets of model parameters and the relative stability for others. The effect is shown in Fig. 5. We consider two exemplary sets of parameters. In the first set (upper panel in Fig. 5), the spot brightness decreased with the radius as $\beta_{\text{rad}} = 3$, in the second set with $\beta_{\text{rad}} = 2$. Again, we choose the mean number of clouds in each model in such a way as to have roughly the same level of variability. For a specific choice of the other parameters (the same for the two models; see caption of Fig. 5), we have to assume $n_{\text{mean}} = 125$ for the first model and $n_{\text{mean}} = 30$ for the second one.

For both parameter sets, we obtained five 300-ks-long time sequences and calculated F_{var} for each of the sequences independently. For clarity, the expected statistical one sigma errors are marked for one of the curves only. The curves in the upper panel are roughly similar, and they do not differ more from each other than expected from simple error analysis. However, the curves in the lower panel differ rather widely. This demonstrates that, for such a set of parameters, a single lightcurve of a standard length and with a standard error description cannot be used to estimate whether the model well represents any specific data. The effect is still somewhat stronger for our data covering only 100 ks instead of 300 ks, as was adopted in these simulations.

The discrepancy is due to the different total mean numbers of flares required by the two data sets. Since

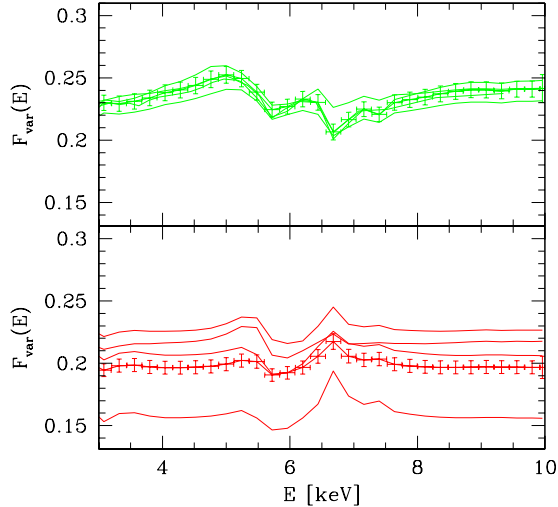


Fig. 5. Fractional variability calculated from several lightcurves calculated for the same model, with the formal errors displayed for one of the curves. Upper panel: $n_{\text{mean}} = 125$, $\beta_{\text{rad}} = 3$; lower panel: $n_{\text{mean}} = 30$, $\beta_{\text{rad}} = 2$. Other model parameters: $M = 10^7 M_{\odot}$, $a = 0.95$, $L_X = 8 \times 10^{43}$ erg s $^{-1}$, $i = 30^\circ$, $R_{\text{out}} = 50 R_{\text{g}}$, $\gamma_{\text{rad}} = 0$, $\delta_{\text{rad}} = 1.5$, $t_{\text{life}_0} = 2 \times 10^4$ s, $T_{\text{obs}} = 6146$ s, and $N = 50$. No primary contribution is assumed.

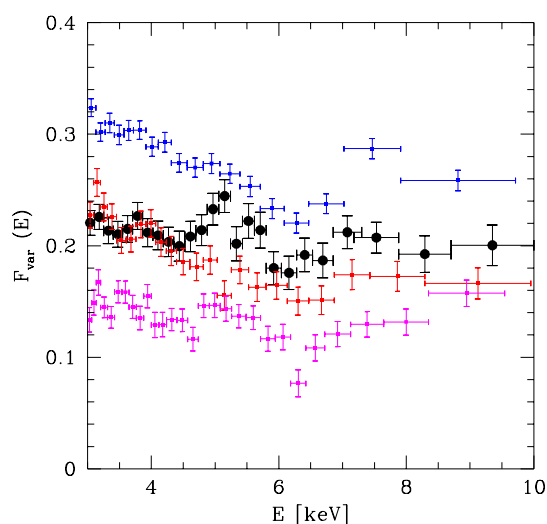


Fig. 6. Fractional variability calculated independently for three separate parts of the 300 ks lightcurve of MCG-6-30-15 (XMM-Newton data, 2001, thin points). The set with filled circles represents the result obtained from the 100 ks lightcurve (XMM-Newton data, 2000). The length of a time bin equals 6146 s.

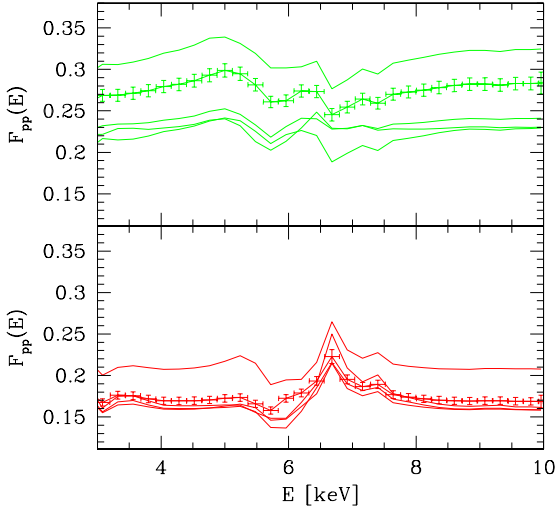


Fig. 7. Point-to-point fractional variability calculated for the same models and displayed in the same manner as the fractional variability shown in Fig. 5.

the flare duration distribution was the same in the two models the total (time-integrated) number of flares in the lightcurve is 726 for the first set of parameters and only 174 for the second set. The standard determination of the statistical error (see Eqn. A.2 of Ponti et al. 2004 and Eqn. 6 in this paper) of course does not include this effect. This result supports the conclusion of Vaughan et al. (2003), based on Monte Carlo simulations of lightcurves with an assumed power spectrum, that the overall normalization of the variance is rather unreliable if based on short observations. However, our energy-dependent calculations indicate that although the *overall level* of the F_{var} changes strongly for some sets of parameters, the *shape* of F_{var} varies less from sequence to sequence. The energy pattern is roughly preserved and can be used to estimate the source properties.

Since our conclusion is based on a specific flare/spot model, we compare the trend to the sampling effects in real data: in Fig. 6 we show three $F_{\text{var}}(E)$ plots obtained by the division of a single 300 ks long lightcurve of MCG-6-30-15 (XMM-Newton observation performed in 2000, see Fabian et al. 2002) into three equal parts. $F_{\text{var}}(E)$ was calculated for each of the three parts independently. The overall change in the variability level between the three subsequences is in good agreement with the expected power red leak for the source. Table 1 of Vaughan et al. (2003) for a source with a PSD slope of 1.0 below the break and 2.0 above the break, for 20 data points, predicts the scatter between -0.71 and 0.45 in logarithm of the variance, so between -0.36 to 0.23 in logarithm of dispersion. This means that the average value of 0.2 is predicted to fluctuate between 0.09 and 0.33, as observed (see Fig. 6).

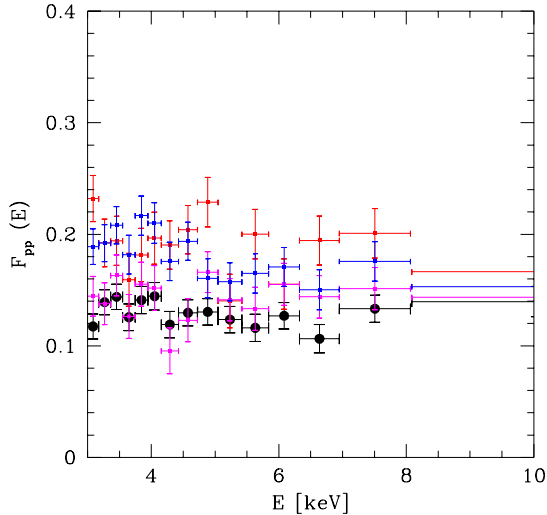


Fig. 8. Point-to-point fractional variability calculated independently for three separate parts of the 100 ks lightcurve of MCG-6-30-15 (XMM-Newton data, 2000, thin points). The set with filled circles represents the mean result obtained directly from the whole lightcurve. The length of a time bin equals 1000 s.

However, most of the variability is in the overall normalization of $F_{\text{var}}(E)$; the shape actually varies much less, although some changes in energy dependence are also seen. The variability is always suppressed just above 6 keV, but one of the data sets does not show the complex structure in 4 - 6 keV band.

The structure of the $F_{\text{var}}(E)$ spectrum of MCG-6-30-15 shown in Fig. 6 is quite typical for Seyfert galaxies. The suppression around 6 keV is often found to be even more pronounced than for this particular object (see, e.g., Markowitz, Edelson, & Vaughan, 2003, for some examples). Another important feature of the rms spectra is an increase of the variability in the soft X-ray band. An interesting interpretation of this feature is proposed by Chevallier et al. (2006). According to this idea, the enhanced soft X-ray variability is due to the response of the warm absorber to the variations of the incident flux. Absorption is most efficient around ~ 1 keV and the change of the ionization state of the warm absorber in the response to the variable flux amplifies the overall variability level in this spectral band. This leads to an increase in the simulated fractional variability amplitude at about that energy.

We also analyze the scatter in point-to-point fractional variability amplitude predicted by the model. The result is shown in Fig. 7. It is interesting to note that the results are complementary to the results for the simple fractional variability. While in Fig. 5 there is much more scatter in the upper panel, in Fig. 7 the trend is reversed. This com-

plementarity is connected with the presence of relatively more (or less) power in a given model at longer timescales. Also, in this case, the model predicts much less variability in the shape than in the overall normalization. In the observed F_{pp} , calculated separately for three parts of the lightcurve, we notice considerable variations in the normalization, although lower than for F_{var} (see Fig. 8). We see some variations of the shape as well, but the basic pattern remains the same. There is a decrease of the variability at ~ 6 keV, which is present in all three sequences, although in one of them it is shifted from 6.6 keV to 6.0 keV. It is difficult to discuss the significance of such variations since the errors are large, although the number of bins was relatively high due to the choice of short time bin (1000 s).

This analysis shows that the observational errors are actually much larger than indicated by a simple statistical analysis of a given single lightcurve, as is expected from the power leaking (Vaughan et al. 2003). However, the errors in the shape are not as large as the overall change of fractional variability amplitude from one to another time sequence, due to the long timescales present in the system. Of course, an increase of the duration of the observation time would give less scatter. But then, such requirements may be difficult to meet. The model from the lower panel of Fig. 5 gives results for F_{var} that are almost within the statistical errors of a single lightcurve, if the number of time bins is increased to $N = 300$. This corresponds to an observation of more than 20 days.

3.3.3. Best representations of $F_{\text{pp}}(E)$

In Fig. 9, we show the point-to-point fractional variability amplitude of MCG-6-30-15 and the best representation of the short timescale variability from our model. The model well represents the suppression of the variability near the core of the iron line, in the 3-10 keV energy band. The position of the minimum in the theoretical plot is basically determined by the inclination angle, and apparently, the value of 30° adopted in most simulations is appropriate. Inclinations smaller than $\sim 10^\circ$ or larger than $\sim 40^\circ$ are excluded.

The width of the dip is mostly determined by the Kerr metric parameter a . Fast rotation of the black hole results in a broad feature extending far to the red side of the line core, while a slowly rotating black hole gives a narrow feature. The value $a = 0.95$, relatively high, but still significantly lower than the maximally rotating black hole, best represents the data. A slower rotation than $a \sim 0.8$ is not consistent with the data. The depth of the feature mostly depends on the ratio of the spot spectrum to the primary emission going towards an observer. Our best representation was obtained assuming no primary contribution, but the contribution of the primary at some level is allowed, as analyzed in detail in Sect. 3.3.5. The overall level of the variability depends mostly on the mean number of flares, and this can always be adjusted if the energy-dependent

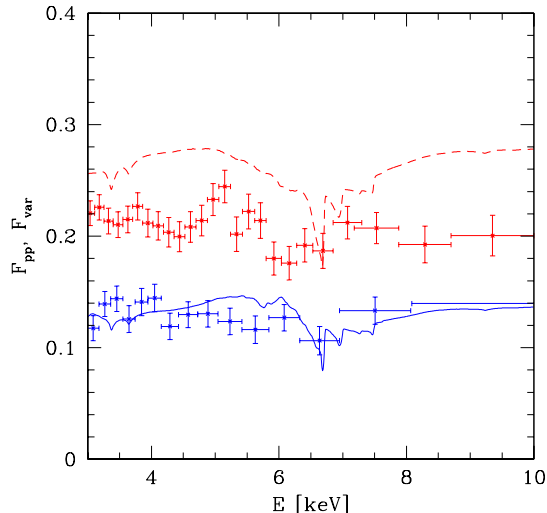


Fig. 9. The best model of F_{pp} (continuous line) with the corresponding data (lower set of points). The upper data set represents F_{var} and the modeling result for the same parameter set: $\beta_{\text{rad}} = 4$, $\gamma_{\text{rad}} = 0$, $\delta_{\text{rad}} = 1.5$, $t_{\text{life}_0} = 2 \times 10^4$ s, and $n_{\text{mean}} = 750$. The other parameters are at their standard values (see caption of Fig. 3). The model is shown unbinned for better clarity.

shape of the F_{var} is appropriate. However, the same model parameters do not represent the F_{var} well.

3.3.4. Best representations of $F_{\text{var}}(E)$

In Fig. 10, we show the best representation of the standard $F_{\text{var}}(E)$ for the source. It roughly reproduces the observed ‘wiggles’ of the F_{var} obtained from the whole lightcurve. However, this time the same parameters do not reproduce F_{pp} correctly. Since there is a considerable randomness in the modeling process, we repeated the computations several times for a different random seed of the Monte-Carlo routines. But in all such realizations, the F_{pp} shows an excess at 6.4 keV instead of a dip. A discrepancy with the data therefore remains.

To decide which set of parameters better represents the source properties, we plot the spectra and the lightcurves from the two models (see Fig. 11). The spectra of both models are quite comparable and do not help to differentiate between the candidate models. The lightcurves, on the other hand, have a rather different character visually (see Fig. 12). The upper curve shows less short time-scale flickering and seems to be quasi-periodic, while the lower curve looks more similar to the source X-ray lightcurve (see Fig. 1 in Ponti et al. 2004).

Therefore, we consider the set of parameters used for Fig. 9 as a more satisfactory description of the variability in MCG-6-30-15.

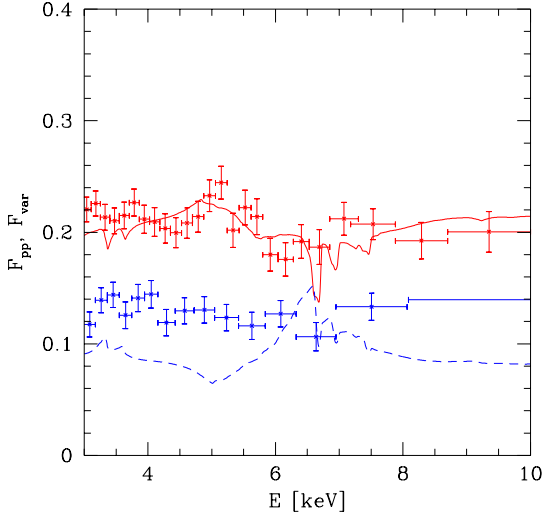


Fig. 10. The best model of F_{var} (continuous line) with the corresponding data (upper set of points). The lower data set represents F_{pp} and the modeling result for the same parameters: $\beta_{\text{rad}} = 3$, $\gamma_{\text{rad}} = 0$, $\delta_{\text{rad}} = 1.5$, $t_{\text{life}_0} = 2 \times 10^5$ s, and $n_{\text{mean}} = 100$. The other parameters are at their standard values (see caption of Fig. 3). The model is shown unbinned for better clarity.

3.3.5. Contribution of the primary emission

To directly compute observable characteristics, we need to combine the primary continuum with the reflected component. The resulting signal depends on the mutual proportion of the two components, and also on the energy range and time resolution of the observation. This means that the degree of anisotropy of the primary flare should be taken into account. Our modeling shows that, if the primary power law emission strongly dominates over the reprocessed component, and if the slope of the primary emission does not change with time, there is no energy-dependence in the fractional variability amplitude. Moderate contribution of the primary results in flattening of the energy dependence without changing the overall variability amplitude. We note, though, that this is only true for the case of a well-defined correlation between the primary and the reprocessed component. This correlation implies that the flare geometry shown in Fig. 1 is the same for all flares distributed over the disk. In reality, these things are likely to be more complicated. If the primary emission and the reprocessing are not perfectly correlated, the overall level of the variability goes down when the primary component becomes more significant.

We calculate examples of the model shown in Fig. 9 with different levels of primary contribution and assuming that both components are well-correlated. We also calculate the equivalent width of the iron line in the resulting

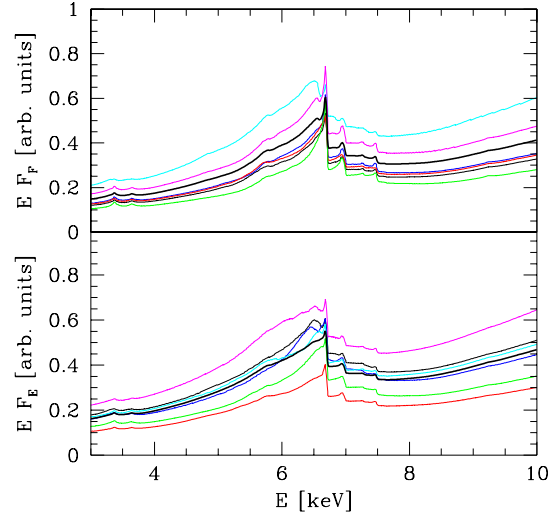


Fig. 11. The spectra at various moments computed from the models shown in Fig. 9 (lower panel) and Fig. 10 (upper panel), with the mean spectra over-plotted by a thick line.

Table 1. Equivalent widths (EW) of the iron line complex and the ratio $F_{\text{pp}}(6 \text{ keV})/F_{\text{pp}}(6.6 \text{ keV})$ as a function of the amount of reflection. The observed $F_{\text{pp}}(6 \text{ keV})/F_{\text{pp}}(6.6 \text{ keV})$ ratio is 1.19, and the model results were binned into the same energy channels as the data.

\mathcal{R}	$EW^a[\text{eV}]$	$EW^b[\text{eV}]$	$F_{\text{pp}}(6 \text{ keV})/F_{\text{pp}}(6.6 \text{ keV})$
∞	1670	1350	1.17
4	660	510	1.14
2	420	320	1.09
1	240	180	1.06

^a measured in the 3 - 8 keV range, ^b measured in the 4 - 9 keV range, with the continuum determined outside the iron line complex.

spectra. These results are shown in Table 1. The model without any primary contribution (anisotropy parameter $\mathcal{R} = \infty$) best represents the decrease of the variability at ~ 6.6 keV, but the EW of the iron line complex in the predicted mean spectra is very large, as can be seen in Fig. 11. The reflection amplitude $\mathcal{R} \sim 4$ is still roughly acceptable from the point of view of the variability. The actual measurements of the line EW in MCG-6-30-15 gave values ranging from 800 eV to 250 eV, depending on the assumption about the underlying continuum (Wilms et al. 2001), and Reynolds et al. (2004) obtained the value of 500^{+300}_{-200} eV, so the line intensity is not strongly overestimated. The model with $\mathcal{R} = 2$ seems to have too low of an energy dependence in the fractional variability amplitude, and for $\mathcal{R} = 1$ it underestimates the line intensity as well.

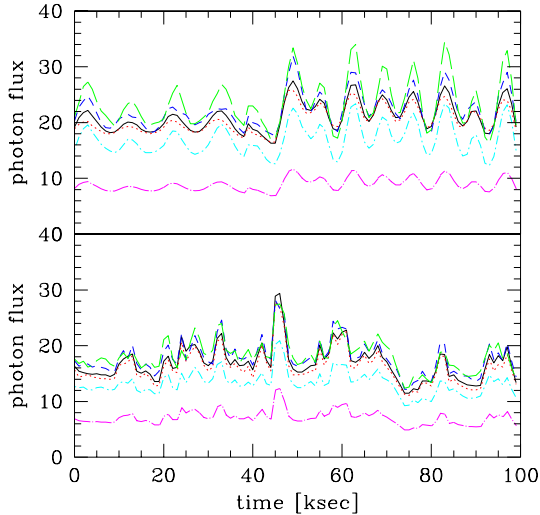


Fig. 12. The lightcurves of the models shown in Fig. 9 (lower panel) and Fig. 10 (upper panel) for narrow energy bands around 4.4 keV, 5.2 keV, 6 keV, 6.4 keV, 6.8 keV, and 8.8 keV, and with the resolution used for the F_{pp} computations.

The amount of reflection can be estimated from the strength of the Compton hump seen in hard X-ray data. The analysis of Beppo-SAX data by Ballantyne et al. (2003) showed that the reflection factor determined from PEXRAV was $R = 2.7^{+1.4}_{-0.9}$ for solar abundances. Assuming higher iron abundance than solar improved the fit and only gave a lower limit to the reflection factor ($R > 2.6$) so the spectrum can actually be reflection-dominated, as advocated for NLS1 (including MCG-6-30-15) by Fabian et al. (2002). A purely reflection-dominated spectrum ($R > 3$) for MCG-6-30-15 was also considered by Taylor, Uttley, & McHardy (2003). Therefore, from the point of view of the primary contribution, the favored model is satisfactory.

4. Discussion

The X-ray spectra of a number of AGN contain a reflection feature which is best modeled as a relativistically smeared iron line (for a review, see, e.g., Reynolds & Nowak 2003). If the source of the irradiation consists of multiple localized flares, it is natural to expect the variability of a single spot luminosity (e.g. Abramowicz et al. 1991; Bao 1992; Karas et al. 1992), as well as of the line shape (Ruszkowski 2000; Nayakshin & Kazanas 2001; Turner et al. 2002; Iwasawa, Miniutti, & Fabian 2004).

In the present paper, we studied in detail the time-dependent spectra from a multi-flare model, paying particular attention to the energy-dependent fractional variability amplitude as a diagnostic tool. We used both the standard fractional variability amplitude, F_{var} , and

the point-to-point fractional variability amplitude, F_{pp} . We showed that the model explains a decrease in the variability level at ~ 6.5 keV derived from the rms-spectra of Seyfert galaxies, such as MCG-6-30-15 (Inoue & Matsumoto, 2001; Vaughan & Fabian, 2004; Ponti et al., 2004). Similar behavior was observed in Mrk 766 (Pounds et al., 2003), 3C 120, Akn 564, IC 4329a, 3C 390.3, Fairall 9, NGC 3516, NGC 3783, NGC 4151, NGC 5548, or NGC 7469 (Markowitz, Edelson, & Vaughan, 2003).

The overall variability level, predicted by the multi-flare model and expressed in terms of F_{var} and F_{pp} , depends strongly on the adopted number of flare-spots. By adjusting this number, the model is capable of reproducing the overall normalization of observed rms-spectra as we demonstrated for the case of MCG-6-30-15. However, the form of the energy dependence of F_{var} and F_{pp} is more difficult to adjust and provides a strong diagnostic tool either for proof or for falsification of our model.

The prediction of the multi-flare model for the shape of F_{var} and F_{pp} depends predominantly on the radial profile of the energy dissipation characterizing a given set of parameters (see Sect. 3.2). If the energy dissipation in the form of flares weighted within the emission area decreases with the radius, the model shows a suppression of the variability at 6.6 keV.

The present data predict both F_{var} and F_{pp} with significant error, mostly due to the presence of the timescales much longer than a typical lightcurve duration (e.g. Vaughan et al. 2003). The errors in the shape of the energy dependence seem to be lower, but still rather difficult to determine observationally. Therefore, we did not provide formal fits to the observational data at the present stage. Instead, we favored one of the studied sets of parameters at the basis of semi-quantitative analysis.

4.1. Best model properties for MCG-6-30-15

The parameters of the model which we considered satisfactory (see Fig. 9) are interesting. The distribution of the timescales was Keplerian, and the requested normalization leads to a timescale range from 1910 s in the innermost part to 8.7×10^4 s in the outermost part. The spot size obtained was $R_X = 1.96 R_g$, which is not too large in the context of the underlying model assumptions. It corresponds to a height of the flare source above the disk equal to $1.13 R_g$. The mean number of coexisting flares is quite large (750), but the variability is nevertheless observed to be that large since most of the luminosity comes only from the few innermost flares. This is due to the rather steep increase of the flare luminosity toward the disk center ($\beta_{\text{rad}} = 4$). Interestingly, the obtained mean number of flares is not unlike the numbers of clouds obtained in the obscurational variability model of Abramart & Czerny (2000).

The steep flare emissivity mentioned above is indeed higher than might be expected just from the shape of the gravitational potential. However, modeling of the mean

shape of the broad iron line frequently required an enhanced emissivity profile (e.g. Wilms et al. 2001). It was also predicted by a theoretical corona model of Kawanaka et al. (2005).

Although the mean number of the coexisting flares is large, we see occasional large ‘single’ flares in the theoretical lightcurve. Such resolved single flares are already seen occasionally in the present data (e.g. Ponti et al. 2004 for MCG-6-30-15). Turner et al. (2005) identified a single orbiting flare in Mrk 766 on the basis of the spectral analysis, and Porquet et al. (2004) also considered a localized flare as a plausible explanation of the ESO 113-G010 spectrum.

4.2. Model approximations

There are still certain inconsistencies present in our model, mainly in the computation of the local spectra. The calculations were made for a Schwarzschild black hole of 10^8 solar masses. However, in computing the relativistic effects, we also use them for other values of M . For MCG-6-30-15, a smaller mass is more appropriate. In our computations of the relativistic effects, we assumed $10^7 M_\odot$ for the mass of the central black hole, and McHardy et al. (2005) suggested an even smaller value $\sim (3-6) \times 10^6 M_\odot$. However, we do not expect any strong direct dependence of the local spectrum on the black hole mass.

The local computations were performed at a single radius ($18R_g$), but we checked that the local spectra calculated at $7R_g$ do not differ strongly (Goosmann et al. 2006) when computed for the same flare-to-disk-flux ratio below the flare. Therefore, for models calculated with this ratio preserved (i.e., models with $\beta_{\text{rad}} = 3$) we do not think we introduce much of an error. However, for models with different β_{rad} the local spectrum may be different, so a range of local models should actually be calculated to incorporate this effect.

The assumptions about the primary radiation in our model are rather simple. The distance between the flare source and the hot spot is assumed to be negligibly small so that the relativistic effects acting on the incident radiation can be neglected. In Goosmann et al. (2006), we show that this is a good approximation for Schwarzschild black holes. For Kerr black holes it works fine if the flares do not get closer to the black hole than $\sim 3R_g$. The primary source is assumed to turn on and off instantaneously and, consequently, so are the hot spots. We thereby assume that the time for the actual reprocessing of the radiation in the disk medium is negligible. The local lightcurve of the spot emission hence has a simple box shape. We keep this assumption, although it is probably too simple, since not much is known yet about the actual production of the primary radiation and its time evolution during a magnetic reconnection event. In later developments of the model, more detailed assumptions about the nature of the flare source should be included. Also the ratio of the primary flux to the disk flux is somehow arbitrarily set to 144 at the spot center. In future work, this flux ratio should be

treated as a free parameter, but of course this requires a large grid of calculations for the local spectrum.

4.3. Power spectrum

The power spectrum derived by McHardy et al. (2005) for MCG-6-30-15 shows a bending, characterized by the break frequency 3.2×10^{-5} Hz, and the asymptotic slopes of -0.8 and -1.74 if the broken power law description is used. It is not clear that our model is able to reproduce its properties. We attempted to calculate the power spectrum from our theoretical lightcurves, but the result was consistent with white noise. This may be partially due to the fact that: (i) the lightcurves contained only a limited number of points (100), and (ii) the studied dynamical range of the model ($R_{\text{out}} = 50 R_g$) is not yet fully satisfactory.

On the other hand, our model in its present version may not contain enough power in the long frequency range. Generally, more complex models involving correlated avalanches of flares are used to model the power spectra in AGN and galactic sources (e.g. Poutanen & Fabian 1999; Zycki 2003; Zycki & Niedzwiecki 2005). A successful model accounting for the power spectrum has to explain why there is a lot of power in the low frequency part of the power spectrum, while most of the energy dissipation takes place in the innermost part where the expected timescales are short.

Two essentially similar models were proposed which can explain the presence of the long timescales successfully: ‘self-organized criticality’ (Mineshige et al. 1994), and ‘traveling perturbations’, (Lyubarskii 1997). Both conclude that the disk accretion rate is locally perturbed, and this perturbation propagates inward, so the accretion rate at any disk radius contains a history of long timescale perturbations created at larger radii. In particular, the model of Lyubarskii (1997) looks natural within the frame of the magneto-rotational instability mechanism of viscosity, and it is particularly appropriate for a power spectrum with a single break like that of MCG-6-30-15.

Our flare model, at present, does not include this kind of perturbation memory. However, in principle, this kind of non-local perturbation of the disk accretion rate can be incorporated into the model. If it is combined with some assumptions of scaling between the local momentary accretion rate and a flare luminosity, it will probably provide the missing power at long timescales.

4.4. Other models of X-ray variability

We have found that our multi-flare model with a time-independent shape of the energy spectrum of the flare emission provides an interesting interpretation of the drop in the variability around 6.5 keV. However, there are other models under discussion.

The energy-dependent form of the variability was also modeled as a variable primary emission with constant reflection (e.g. Taylor, Uttley, & McHardy, 2003; Shih,

Iwasawa, & Fabian, 2002), or as a result of the pivoting of the primary power law emission (e.g. Markowitz, Edelson, & Vaughan, 2003).

However, in this first class of models it is difficult to explain why the reflection component should be constant since either it forms close to the black hole (and the source of the primary emission) and should respond to changes of the primary, or it forms far away, then it is difficult to explain why it is relativistically broadened. An attractive way out of this paradox was proposed by Martocchia, Karas, & Matt (2000); Miniutti & Fabian (2004); and Miniutti et al. (2005), who describe a model where the change in the primary intensity is predominantly due to the minor changes in the position of the source of the primary radiation at the disk rotation axis, which gave effects strongly enhanced due to the general relativity. Pivoting is also quite natural, if the flare evolution (cooling, expansion) is taken into account. However, in this case the drop in the variability level can be at any position, and not just around the iron line complex.

There are also entirely different models of the X-ray variability of AGN, for example the presence of the density inhomogeneities in the disk atmosphere resulting from the photon bubble instability (Ballantyne et al. 2005), developments of the temporary spiral structures in the accretion disk (Fukumura & Tsuruta 2005), variations in the properties of the warm absorber (e.g. Sako et al. 2002; Done & Gierlinski, 2006, private communication), or variations in the the inner disk torque (Garofalo & Reynolds 2005). Only more detailed studies of model predictions and comparison with the data in more than just one aspect may bring a reliable answer to the true nature of the X-ray variability.

Acknowledgements. Part of this work was supported by the grants PBZ-KBN-054/P03/2001 and 4 T12E 047 27 of the Polish State Committee for Scientific Research, by the Laboratoire Européen Associé Astrophysique Pologne-France, by the CNRS GDR PCHE, by the Hans-Böckler-Stiftung in Germany (RWG), and by the Center of Theoretical Astrophysics in Czechia. The authors gratefully acknowledge support from the Czech Science Foundation GACR 202/06/0041 (VK) and 205/05/P525 (MD). The Astronomical Institute in Prague has been operated under the project AV0Z10030501. GP thanks the European commission under the Marie Curie Early Stage Research Training program for support.

References

- Abramowicz M. A., Bao G., Lanza A., & Zhang X.-H. 1991, *A&A*, 245, 454
- Abrassart A., & Czerny B. 2000, *A&A*, 356, 475
- Ballantyne D. R., Turner N. J., & Young A. J. 2005, *ApJ*, 619, 1028
- Ballantyne D. R., Ross R. R., & Fabian A. C. 2001, *MNRAS*, 327, 10
- Ballantyne D. R., Vaughan S., & Fabian A. C. 2003, *MNRAS*, 342, 239
- Bao G. 1992, *A&A*, 257, 594
- Beloborodov A.M. 1999, *ApJ*, 510, L123
- Bisnovatyi-Kogan G. S., & Blinnikov S. I. 1977, *A&A*, 59, 111
- Chevallier L., Czerny B., Collin S., & Różańska, A., 2006, submitted to *A&A*
- Collin S., Coupé S., Dumont A.-M., Petrucci P.-O., & Różańska A. 2003, *A&A*, 400, 437
- Cui W., Zhang S. N., Focke W., & Swank J. H. 1997, *ApJ*, 484, 383
- Czerny B., Nikolajuk M., Rozanska A., Dumont A.-M., Loska Z., & Zycki P.T. 2003, *A&A*, 412, 317
- Czerny B., & Elvis M. 1987, *ApJ*, 321, 305
- Czerny B., & Goosmann R. 2004, *A&A*, 428, 39
- Czerny B., Różańska A., Dovciak M., Karas V., & Dumont A.-M. 2004, *A&A*, 420, 1
- di Matteo T. 1998, *MNRAS*, 299, L15
- Dovciak M., Karas V., & Yaqoob T. 2004, *ApJSS*, 153, 205
- Dovciak M. 2004, Radiation of accretion disks in strong gravity, PhD-thesis
- Dumont A.-M., Collin S., Paletou F., Coupé S., Godet O., & Pelat D. 2003, *A&A*, 407, 13
- Dumont A.-M., Czerny B., Collin S., & Zycki P. T. 2002, *A&A*, 387, 63
- Dumont A.-M., Abrassart A., & Collin S. 2000, *A&A*, 357, 823
- Edelson R., Turner T. J., Pounds K. A., Vaughan S., Markowitz A. et al. 2002, *ApJ*, 568, 610
- Fabian A. C., Miniutti G., Iwasawa K., & Ross R. R. 2005, *MNRAS*, 361, 795
- Fabian A. C., Vaughan S., Nandra K., Iwasawa K., Ballantyne D. R. et al. 2002, *MNRAS*, 335, L1
- Fabian A.C., Ballantyne D., Mirloni A., Vaughan S., Iwasawa K., & Boller Th. 2002, *MNRAS*, 331, L35
- Field G.B. 1965, *ApJ*, 142, 431
- Fukumura K., & Tsuruta S. 2004, *ApJ*, 613, 700
- Galeev A. A., Rosner R., & Vaiana G. S. 1979, *ApJ*, 229, 318
- Garofalo D., & Reynolds C.S. 2005, *ApJ*, 624, 94
- Gilfanov M., Churazov E., & Revnivtsev, M. 2000, *MNRAS*, 316, 923
- Goosmann R. W., Czerny B., Mouchet M., Dumont A.-M., Karas V., & Dovciak M. 2006, in preparation
- Haardt F., & Maraschi L. 1991, *ApJ*, 380, 51
- Haardt F., Maraschi L., & Ghisellini G. 1994, *ApJ*, 432, 95
- Henri G., & Pelletier G. 1991, *ApJ*, 383, L7
- Ichimaru S. 1977, *ApJ*, 214, 840
- Inoue H., & Matsumoto C. 2001, *Adv. Space Res.*, 28, 445
- Iwasawa K., Miniutti G., & Fabian A. C. 2004, *MNRAS*, 355, 1073
- Kaastra J.S. et al. 2004, *A&A*, 422, 97
- Karas V., Vokrouhlický D., & Polnarev A.G. 1992, *MNRAS*, 259, 569
- Kato Y., Mineshige S., & Shibata K. 2004, *ApJ*, 605, 307
- Kawanaka N., Mineshige S., & Iwasawa K. 2005, *ApJ*, 635, 167
- King A. R., Pringle J. E., West R. G., & Livio M. 2004, *MNRAS*, 3478, 111
- Ko Y.-K., & Kallman T.R. 1994, *ApJ*, 431, 273
- Krolik J. H., McKee C. F., & Tarter C. B. 1981, *ApJ*, 249, 422
- Lachowicz P., & Czerny B. 2005, *MNRAS*, 361, 645
- Lawrence A., Watson M. G., Pounds K. A., & Elvis M. 1987, *Nat.*, 325, 649
- Lehto H. J. 1989, *ESA SP-296: Two Topics in X-Ray Astronomy*, Volume 1: X Ray Binaries. Volume 2: AGN and the X Ray Background, ed. Hunt J., & Battwick B., p. 499
- Liang E. P., & Price R. H. 1977, *ApJ*, 218, 427

- Lightman A. P., & White T. R. 1988, *ApJ*, 335, 57
- Lyubarskii Yu. E. 1997, *MNRAS*, 292, 679
- Markoff S., Nowak M. A., & Wilms J. 2005, *ApJ*, 635, 1203
- Markowitz A. 2005, *ApJ*, 635, 180
- Markowitz A., Edelson R., & Vaughan S. 2003, *ApJ*, 598, 935
- Markowitz A. et al. 2003, 593, 96
- Martocchia A., Karas V., & Matt G. 2000, *MNRAS*, 312, 817
- McHardy I.M., & Czerny B. 1987, *Nat.*, 325, 696
- McHardy I.M., Gunn K.F., Uttley P., & Goad M.R. 2005, *MNRAS*, 359, 1469
- Merloni A. 2003, *MNRAS*, 341, 1051
- Merloni A., & Fabian A.C. 2001, *MNRAS*, 328, 958
- Miller K.A., & Stone J.M. 2000, *ApJ*, 534, 398
- Mineshige S., Ouchi N.B., & Nishimori H. 1994, *PASJ*, 46, 97
- Miniutti G., & Fabian A. C. 2004, *MNRAS*, 349, 1435
- Miniutti G., Fabian A. C., Goyder R., & Lasenby A. N. 2003, *MNRAS*, 344, L22
- Miyamoto S., Kitamoto S., Kazuhisa M., & Dotani T. 1988a, *Nature*, 336, 450
- Narayan R., & Yi I. 1994, *ApJ*, 428, L13
- Nayakshin S. 2000, *ApJ*, 540, L37
- Nayakshin S., & Kazanas D. 2001, *ApJ*, 553, L141
- Nayakshin S., Kazanas D., & Kallman T.R. 2000, *ApJ*, 537, 833
- Nolan P.L. et al. 1981, *ApJ*, 246, 494
- Ponti G., Cappi M., Dadina M., & Malaguti G. 2004, *A&A*, 417, 451
- Porquet D., Reeves J.N., Uttley P., & Turner T.J. 2004, *A&A*, 427, 101
- Pounds K. A., Reeves J. N., Page K. L., Wynn G. A., & O'Brien, P. T. 2003, *MNRAS*, 342, 1147
- Pounds K. A. 1985, in *Galactic and Extra-Galactic Compact X-ray Sources*, proceedings of the Japan-US Seminar, January 1985, ed. Tanaka Y., & Lewin H. G., p. 261
- Poutanen J., & Fabian A.C. 1999, *MNRAS*, 306, L31
- Raymond J. C. 1993, *ApJ*, 412, 267
- Reynolds C. S., & Nowak M. A. 2003, *Phys. Rep.*, 377, 389
- Reynolds C. S., Wilms J., Begelman M. C., Taubert R., & Kendziorra E. 2004, *MNRAS*, 349, 1153
- Ross R. R., & Fabian A. C. 1993, *MNRAS*, 261, 74
- Ross R. R., Fabian A. C., & Young A. J. 1999, *MNRAS*, 306, 461
- Rózańska A., Dumont A.-M., Czerny B., & Collin S. 2002, *MNRAS*, 332, 799
- Rózańska A., & Czerny B. 1996, *Acta Astr.*, 46, 233
- Ruszkowski M. 2000, *MNRAS*, 315, 1
- Sako M., Kahn S. M., Paerels F., Liedahl D. A., Watanabe, S., Nagase, F., & Takahashi, T. 2002, in *High Resolution X-ray Spectroscopy with XMM-Newton and Chandra*, proceedings of the international workshop held at the Mullard Space Science Laboratory of University College London, United Kingdom, October 24 - 25, ed. Branduardi-Raymont G., p. 191
- Sobolewska M., Siemiginowska A., & Zycki P. T. 2004a, *ApJ*, 608, 80
- Sobolewska M., Siemiginowska A., & Zycki P. T. 2004b, *ApJ*, 6017, 102
- Shih D. C., Iwasawa, K., & Fabian, A. C. 2002, *MNRAS*, 333, 687
- Stern B. E., Poutanen J., Svensson R., Sikora M., & Begelman M. C. 1995, *ApJL*, 449, L13
- Taylor R. D., Uttley P., & McHardy I. M. 2003, *MNRAS*, 342, L31
- Torricelli-Ciamponi G., & Pietrini P., Orr A. 2005, *A&A*, 438, 55
- Turner N. J. 2004, *ApJ*, 605, L45
- Turner T. J., Miller L., George I. M., & Reeves J. N. 2005, *A&A*, 445, 59
- Turner T. J. et al. 2002, *ApJ*, 574, L123
- Uttley P., McHardy I. M., & Vaughan S. 2005, *MNRAS*, 359, 345
- Vaughan B. A., & Nowak M. A. 1997, *ApJ*, 474, L43
- Vaughan S., Edelson R., Warwick R. S., & Uttley P. 2003, *MNRAS*, 345, 1365
- Vaughan S., & Fabian A. C. 2004, *MNRAS*, 348, 1415
- Wilms J., Reynolds C. S., Begelman M. C., Reeves J., Molendi S. et al. 2001, *MNRAS*, 328, L27
- Yaqoob T. et al. 2003, *ApJ*, 596, 85
- Zycki P. T. 2002, *MNRAS*, 333, 800
- Zycki P. T. 2003, *MNRAS*, 340, 639
- Zycki P. T., & Czerny B. 1994, *MNRAS*, 266, 653
- Zycki P. T., & Niedzwiecki A. 2005, *MNRAS*, 359, 308